Proceedings of ASME Turbo Expo 2022
Turbomachinery Technical Conference and Exposition
GT2022
June 13-17, 2022, Rotterdam, The Netherlands

GT2022-79369

LOW MACH PRECONDITIONING FOR TURBOMACHINERY FLOW SIMULATIONS WITH CAVITIES AND VARIABLE GAS COMPOSITIONS

Pierre Sivel*
Institute of Propulsion Technology
German Aerospace Center (DLR)
Linder Höhe, 51147 Cologne
Germany
Email: pierre.sivel@dlr.de

Christian Frey
Institute of Propulsion Technology
German Aerospace Center (DLR)
Linder Höhe, 51147 Cologne
Germany
Email: christian.frey@dlr.de

Edmund Kügeler
Institute of Propulsion Technology
German Aerospace Center (DLR)
Linder Höhe, 51147 Cologne
Germany
Email: edmund.kuegeler@dlr.de

Markus Keil
Aerodynamics CFD Methods
MTU Aero Engines AG
Dachauer Straße 665, 80995 Munich
Germany
Email: markus.keil@mtu.de

ABSTRACT

The optimization of turbomachines increasingly relies on highly accurate numerical performance predictions. Loss predictions require the cavities of the machine to be included in numerical simulations. Commonly, in cavities, the velocity of the simulated fluid is small. For density-based solvers, this results in slow convergence and inaccurate computations. Further, the fluid in cavities is often composed of several gases. This paper presents the low Mach preconditioning method for multi-component thermally perfect gas of DLR's inhouse solver TRACE.

Two low Mach academic test cases, a lid driven cavity and an air and exhaust gas mixing layer, are computed to validate the preconditioner. Both test cases show an accelarated convergence and an improved accuracy, when preconditioning is used.

A 1.5 stage low-pressure turbine rig with a labyrinth seal is computed with thermally perfect air. The result shows a good agreement with the experimental reference. The fluid is then changed to exhaust gas, and two air inflows are added in the labyrinth seal, to analyze the effect of low Mach preconditioning on the mixing of the two gases. The preconditioned computation shows an improved convergence in the cavity. Moreover, the wall temperature and the gas distribution in the cavity differ, when preconditioning is applied.

NOMENCLATURE

CFD	computational fluid dynamics
CFL	Courant-Friedrichs-Lewy
NRBC	non-reflecting boundary condition
a	Speed of sound [m/s]
A, B, C	Flux jacobians in x, y and z direction
c_p, c_v	Specific heat capacity [J/kgK]
D	Flux jacobian at face
$\lvert\tilde{D}\rvert$	Roe averaged flux jacobian
e, e_i	Specific internal energy and species' specific internal energy [J/kg]

*Address all correspondence to this author.

E	Specific total energy [J/kg]
F, G, H	Flux vector in x, y and Z direction
$F_\mathrm{L}, F_\mathrm{R}$	Left and right convective face fluxes
h	Specific enthalpy [J/kg]
Δh_min	Smallest cell length [m]
I	Identity matrix
k	Preconditioning constant [-]
l	Domain length [m]
M, M^{-1}	Right and left eigenvector matrix
Ma	Mach number [-]
Ma_in	Inlet Mach number [-]
n_x, n_y, n_z	Face unit normal vector [-]
N	Number of species [-]
p, p_tot	Pressure and stagnation pressure [Pa]
$\lvert\Delta p\rvert$	Absolute pressure difference to neighbouring cells [Pa]
P	Conservative preconditioning matrix
P_S	Entropy primitive preconditioning matrix
$\lvert\tilde{PD}\rvert$	Roe averaged preconditioned flux jacobian
Q	Conservative state vector
$Q_\mathrm{L}, Q_\mathrm{R}$	Left and right face states
Q_S	Entropy primitive state vector
r	Radius [m]
Re_in	Inlet Reynolds number of the turbine [-]
Re_wall	Wall Reynolds number of the lid driven cavity [-]
R, R_i	Mixture and species specific gas constant [J/kgK]
S	Specific entropy [J/kgK]
T, T_tot	Temperature and stagnation temperature [K]
(u, v, w)	Velocity vector [m/s]
u_wall	Wall velocity [m/s]
(x, y, z)	Cartesian position vector [m]
Y_i	Mass fraction [-]
β^2	Preconditioning parameter [-]
β^2_min	Lower limit for the preconditioning parameter [-]
γ	Specific heat ratio [-]
λ	Stoichiometric factor [-]
λ_i	Eigenvalues [m/s]
Λ	Eigenvalue matrix
ν	Kinematic viscosity [m^2/s]
ρ, ρ_i	Density and partial density [kg/m^3]
Ω	Rotational Speed [1/s]
τ	Pseudo-time [s]

INTRODUCTION

With an ever-growing demand for more fuel-efficient aero engines, turbine developers are constantly striving to maximize the efficiency of their designs. Over the past decades, the turbine inlet temperature has steadily been increased to meet this end. To protect the structural integrity of the hot parts downstream of the combustor, sophisticated cooling designs are employed. This in turn produces an increased attention on accurate computational fluid dynamics (CFD) predictions of cooling effects on both turbine performance and temperature distribution along the structure. A thermally perfect gas model can bring the CFD closer to the measurements than the current design standard of a calorically perfect gas [1]. Further, a multi-component gas model is necessary to accurately predict the mixing of hot exhaust gas and fresh cooling air [2].

The turbine design needs to incorporate the cavity setup into the computation to be able to predict the interaction with the main gas path. These parts of the computational domain pose a challenge for density-based solvers because of their low Mach flow regime. Low Mach preconditioning has shown promising results to overcome these difficulties in previous studies [3, 4]. The preconditioned computations exhibited more stability and accelerated convergence.

The combination of thermally perfect gas with variable mixture and preconditioning for low Mach areas would provide an important step in keeping up with the demands of modern turbine design.

Chorin et al. [5] first introduced low Mach preconditioning under the name artificial compressibility method. This method improved the convergence rate of incompressible solvers by introducing a time derivative of the pressure to the continuity equation. Turkel et al. [6], generalized the artificial compressibility method and applied it to the compressible Euler equations, leading to the so called time-derivative preconditioning. Choi and Merkle [7] derived an alternative preconditioning method based on an asymptotic expansion of the Euler equations for vanishing Mach numbers. Later, preconditioning for viscous flows was analyzed, resulting in preconditioners for all Reynolds number ranges [8, 9]. A Choi Merkle type preconditioner was than derived by Weiss and Smith [10] for arbitrary equations of state.

The first low Mach preconditioners for multi-component gas were presented by Venkateswaran et al. [11] and Shuen et al. [12], who expanded the Choi and Merkel preconditioner [8] to compute reactive nozzle flow. The Weiss and Smith preconditioner was extended for multi-component by Li et al. [13], by Neaves and Edwards [14] and by Housman et al. [15] with focus on two-dimensional multi-phase computations. The preconditioning matrix presented by Housman et al. was later successfully applied to three-dimensional test cases by Kiris et. al [16]. The method proposed by Turkel was later extended for reacting flows by Wu and Luke [17] and by Elmahi et al. [18].

Godfrey et al. [19] showed that computations using an unmodified Roe scheme [20] lead to inaccurate results at low Mach numbers. They further proposed for steady computations that the artificial dissipation needed to be calculated based on the preconditioned equations. This approach was later shown to correctly equalize the artificial dissipation and therefore greatly improve the quality of the solution at low Mach numbers [21, 22].

Tweedt et al. [23] successfully applied low Mach preconditioning to a centrifugal compressor, resulting in the first success-

ful application of preconditioning in a turbomachinery computation. Anker et al. [24] proposed an adaptation for non-reflecting boundary conditions (NRBCs) in preconditioned computations that enabled them to compute multistage configurations. They applied the method to a 1.5 stage low-speed test rig. Fiedler et al. [4] analyzed the effects of low Mach preconditioning in a labyrinth seal attached to a 1.5 stage low pressure turbine.

In this paper, the low Mach preconditioning method for perfect gas of DLR's inhouse solver TRACE is extended for thermally perfect multi-component gas. Since the perfect gas preconditioner is based on Turkel's preconditioner [6], it is extended following the method proposed by Elmahi et al. [18]. Elmahi et al. demonstrated the good performance of the preconditioner for reactive and non-reactive two-dimensional test cases. The low Mach preconditioner is now formulated for three-dimensional flow and applied to a realistic three-dimensional turbomachinery test case with cavities and multi-component gas.

The first section of this paper explains the theory of thermally perfect low Mach preconditioning. Then, the capabilities of the preconditioner are validated with a lid driven cavity test case and an academic laminar mixing layer test case. In both cases the preconditioner greatly increases the convergence rate of the computations, while improving the quality of the results. Finally, the method is applied to the "ATRD" low pressure turbine rig with cavities. First, the turbine is computed with air, to show that the results agree well with the experimental data. Then, the main flow is computed with exhaust gas and two air inlets are added in the cavity. Preconditioned computations show an improved convergence in the cavity and in the main flow. Further, the application of low Mach preconditioning results in changes to the structure of the flow inside the cavity. This leads to differences in heat transport in the cavity, which in turn results in different wall temperatures.

LOW MACH PRECONDITIONING

Starting point are the three-dimensional Euler equations for multi-component gas.

$$\frac{\partial Q}{\partial \tau}+\frac{\partial F}{\partial x}+\frac{\partial G}{\partial y}+\frac{\partial H}{\partial z}=0. \tag{1}$$

Here, $Q=(\rho,\rho u,\rho v,\rho w,\rho E,\rho Y_1,\ldots,\rho Y_N)$ is the conservative state vector, where ρ is the density, (u,v,w) is the velocity vector, E is the specific total energy, Y_i is the mass fraction of the ith species and N is the number of species. Further, τ is the pseudo-time and F, G and H are the convective fluxes in the x, y and z direction, respectively.

The flux Jacobian for a face with unit normal vector $n=(n_x,n_y,n_z)$ is $D=n_xA+n_yB+n_zC$, where $A=\partial F/\partial Q$, $B=\partial G/\partial Q$ and $C=\partial H/\partial Q$ are the convective flux Jacobians. The eigenvalues of D are:

$$\lambda_{1,2,3,5+i}=n_xu+n_yv+n_zw \tag{2}$$

$$\lambda_{4,5}=\lambda_1\pm a\|n\|. \tag{3}$$

Here, a is the isentropic speed of sound.

The eigenvalues represent the propagation speeds in the direction of n. The fourth and fifth eigenvalues correspond to the upstream and downstream acoustic speeds, while the remaining eigenvalues correspond to the convective speed. For vanishing Mach number $Ma\to 0$, with

$$Ma=\frac{\sqrt{u^2+v^2+w^2}}{a}, \tag{4}$$

the convective propagation speed tends to zero while the acoustic propagation speeds remain of the order of the speed of sound. Due to this large disparity in propagation speeds, the system of equations becomes stiff, which leads to slow convergence.

One way to remove the stiffness of the system is to apply low Mach preconditioning, also called time-derivative preconditioning. The preconditioning method presented in this paper is based on the artificial compressibility method proposed by Chorin [5] that was generalized by Turkel [6] and expanded for multi-component gas by Elmahi et al. [18].

First the Euler equations are transformed to primitive entropy variables $Q_S=(p,u,v,w,S,Y_1,\ldots,Y_N)$:

$$\frac{\partial Q_S}{\partial \tau}+\frac{\partial F_S}{\partial x}+\frac{\partial G_S}{\partial y}+\frac{\partial H_S}{\partial z}=0. \tag{5}$$

The transformation from conservative variables to primitive entropy variables for multi-component thermally perfect gas are given in the appendix. In this primitive system, for low Mach numbers, the pressure equation decouples from the rest of the system [18]. In accordance to the artificial compressibility method, the coupling of the pressure equation is enforced by scaling the time-derivative of the pressure equation by $\frac{1}{\beta^2}$, where β^2 is a preconditioning parameter. Written as a preconditioning matrix, in entropy primitive variables, the scaling of the time-derivative is

$$P_S^{-1}=\operatorname{diag}\left(\frac{1}{\beta^2},1,1,1,1,1,\ldots,1\right). \tag{6}$$

This leads to the preconditioned equations

$$P_S^{-1}\frac{\partial Q_S}{\partial \tau}+\frac{\partial F_S}{\partial x}+\frac{\partial G_S}{\partial y}+\frac{\partial H_S}{\partial z}=0. \tag{7}$$

The equations can then be transformed back to the conservative system

$$P^{-1}\frac{\partial Q}{\partial \tau}+\frac{\partial F}{\partial x}+\frac{\partial G}{\partial y}+\frac{\partial H}{\partial z}=0. \tag{8}$$

The conservative preconditioning matrix P^{-1} is presented in the appendix.

The eigenvalues of the preconditioned flux jacobian PD are

$$\lambda_{1,2,3,5+i}=n_x u+n_y v+n_z w \tag{9}$$

$$\lambda_{4,5}=\frac{1}{2}\left(\left(1+\beta^2\right)\lambda_1\pm\sqrt{\left(\left(1-\beta^2\right)\lambda_1\right)^2+4\beta^2 a^2\left\|n\right\|^2}\right). \tag{10}$$

While the convective eigenvalues remained unchanged, the acoustic propagation speeds now depend on the choice of β^2.

To remove the stiffness of the system, the propagation speeds need to be equalized, which is equivalent to reducing the ratio of largest to smallest eigenvalues. For $Ma\to 0$, the optimal eigenvalue ratio is obtained if $\beta^2=Ma^2$ [22]. However, for vanishing Ma, the preconditioning matrix becomes singular. Therefore, a user-defined lower threshold $\beta^2_{\min}$ is introduced, which is typically set to 1e-5. For more complex computations it is set to $\beta^2_{\min}=Ma^2_{in}$, where Ma_{in} is the inlet Mach number. Further, β^2 is multiplied by a problem dependent constant k. To further increase the stability, Darmofal and Siu [25] proposed to locally increase β^2, depending on the local pressure difference to neighbouring cells $|\Delta p|$. In the low Reynolds regime, diffusive effects dominate the flow, and therefore also the convergence. By adjusting β^2 to the diffusion velocity $\nu/\Delta h_{\min}$, an optimal convergence is retrieved [10]. Here, ν is the kinematic viscosity and $\Delta h_{\min}$ is the smallest edge length of a cell. Finally, low Mach preconditioning is disabled for supersonic flows by setting $\beta^2=1$. The final definition of β^2 is

$$\beta^2=\min\left(1,\max\left(kMa^2,\frac{\nu^2}{\Delta h^2_{\min}a^2},\frac{|\Delta p|}{\rho a^2},\beta^2_{\min}\right)\right). \tag{11}$$

Apart from slow convergence, density-based solvers produce unphysical solutions for low Mach flows. As shown in e.g [21], the damping terms of the standard Roe scheme do not scale correctly for $Ma\to 0$, which leads to an excessive artificial dissipation. To improve the accuracy of the solver in the low Mach regime, a preconditioned Roe scheme is used to discretize the convective fluxes. Here, the Roe matrix $|\tilde{D}|$ is replaced with a preconditioned Roe matrix $P^{-1}|\tilde{PD}|$. Therefore, the preconditioned convective face flux is

$$F_{\text{face}}=\frac{1}{2}\left(F_{\text{L}}+F_{\text{R}}\right)-\frac{1}{2}P^{-1}|\tilde{PD}|\left(Q_{\text{L}}-Q_{\text{R}}\right), \tag{12}$$

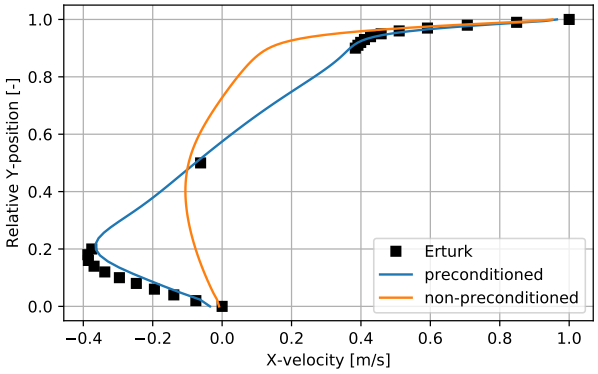

FIGURE 1. X-VELOCITY PROFILE ALONG THE CONSTANT-X CROSS SECTION THROUGH THE CENTER OF THE CAVITY.

where, the subscripts L and R denote the left and right states at the face. The construction of the matrix $P^{-1}|\tilde{PD}|$ is described in the appendix. The viscous fluxes are discretized using a central scheme and do not need any adjustment for preconditioned computations

RESULTS

To validate the preconditioner, a lid driven cavity and a mixing layer of air and exhaust gas at low Mach numbers are computed. Then, the method is applied to a 1.5 stage low pressure turbine rig with a labyrinth seal. The turbine rig was designed by MTU Aero Engines AG in Munich. First, the turbine rig is computed with air to validate the results with experimental data provided by MTU Aero Engines AG. Then, it is computed with exhaust gas and two additional air inlets inside the cavity.

All computations are performed using DLR's inhouse solver TRACE [26, 27]. TRACE is a hybrid multi block RANS solver for structured and unstructured meshes, which solves the Favre- and Reynolds-averaged Navier-Stokes equations. The spatial discretization of the convective fluxes is a second order accurate Roe upwind scheme [20], which is replaced with the preconditioned Roe scheme for preconditioned computations. The viscous fluxes are discretized using a central scheme. The discretized equations are solved using a fully implicit predictor corrector scheme combined with a pseudo time step approach. A symmetric Gauss-Seidel procedure is used to solve the implicit system of equations. All test cases in this paper are computed using a thermally perfect gas model.

Lid Driven Cavity

This academic test case represents a simplified cavity in a labyrinth seal. It is a benchmark case for the validation of low Mach preconditioning methods, which has been thoroughly analyzed by various authors [28, 29].

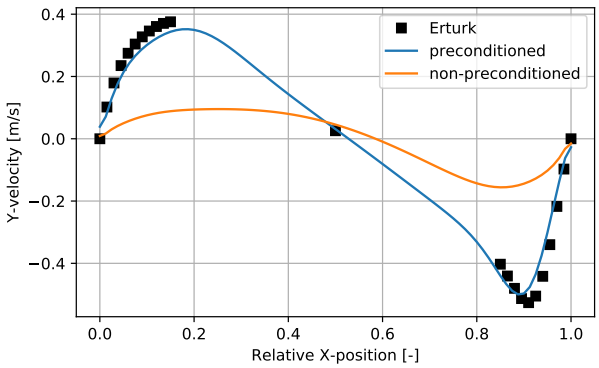

FIGURE 2. Y-VELOCITY PROFILE ALONG THE CONSTANT-Y CROSS SECTION THROUGH THE CENTER OF THE CAVITY.

The cavity consists of a two-dimensional squared domain filled with air. The upper wall of the cavity moves with a velocity of $u_{wall} = 1\,\mathrm{m/s}$, which drives the flow inside the cavity. The mesh of the cavity consists of 41 x 41 cells. The walls are adiabatic and a low Reynolds approach is used. The pseudo time step is computed using a Courant-Friedrichs-Lewy (CFL) number of 100. The initial state is constant in the cavity and is defined as $\rho = 1\,\mathrm{kg/m^3}$, $p = 100\,000\,\mathrm{Pa}$ and $u = v = 0\,\mathrm{m/s}$. Based on the domain length, the upper wall velocity and the initial kinematic viscosity, the wall Reynolds number is $Re_{\mathrm{wall}} = u_{\mathrm{wall}} l/\nu = 1000$. The flow in the cavity is laminar. The lower limit for the preconditioned parameter is $\beta^2_{\mathrm{min}} = 1\text{e-}5$.

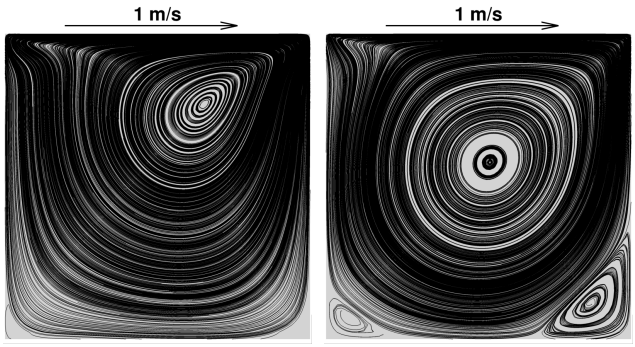

FIGURE 3. STREAMLINES IN THE LID DRIVEN CAVITY AT RE = 1000 WITHOUT (LEFT) AND WITH (RIGHT) PRECONDITIONING.

TABLE 1. MOLAR COMPOSITION OF EXHAUST GAS.

AR	O2	H2O	CO2	N2
0.09	0.1047	0.0654	0.0654	0.7556

Figures 1 and 2 show the x- and the y-velocity profiles through the center of the domain on constant-x and constant-y cross sections, respectively. The results computed with TRACE are compared with the results of Erturk et al. [28], which were computed on a 601 x 601 grid by solving the incompressible Navier Stokes equations. While the preconditioned computation shows a good agreement with the numerical reference, the non-preconditioned computation fails to correctly predict the strength and position of the main vortex in the cavity.

The lid driven cavity test case develops distinct vortex structures depending on the Reynolds number [28]. For a Reynolds number of $Re = 1000$, two vortices form in the lower corners of the domain. Figure 3 depicts the structure of the flow inside the cavity with and without low Mach preconditioning. The preconditioned result, distinctly shows the expected vortices in the corners of the domain, while the non-preconditioned computation fails to predict them.

The preconditioned computation reaches an L1-residual of 1e-11 after 7 364 iterations. Without preconditioning the residual reached the same level of convergence after 225 526 iterations. Preconditioning accelerates the convergence by 97%.

Laminar Mixing Layer

To test the capabilities of the preconditioner to improve the convergence rate and the accuracy of multi-component gas computations a laminar mixing layer of air and exhaust gas is computed.

The computational domain is a 0.55 m long and 0.05 m high channel with an air inlet, an exhaust gas inlet and an outlet. The composition of the exhaust gas is presented in Tab. 1. It corresponds to a simplified exhaust gas composition originating from a lean kerosene combustion at a stoichiometric factor of $\lambda = 2$ [30]. An infinitely thin inviscid wall separates the two inlets for the first 0.05 m. The boundaries in y-direction are inviscid walls. Steady one-dimensional NRBCs [31] are applied at

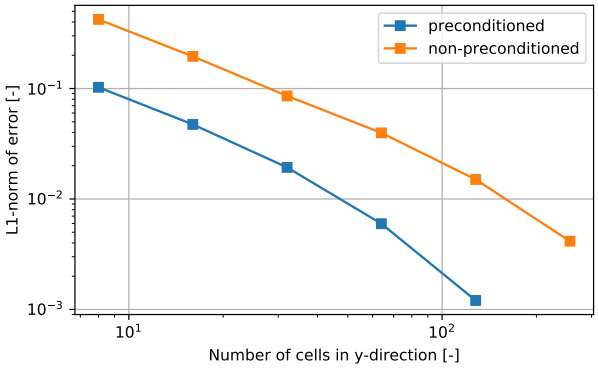

FIGURE 4. L1-NORM OF THE ERROR IN THE AIR MASS FRACTION AT THE OUTLET OF THE DOMAIN.

the inlets and outlet, which have been adapted for preconditioned computations [24]. At both inlets, the stagnation temperature is T_{tot}= 473.14 K and the stagnation pressure is p_{tot} = 101 325 Pa. At the outlet the static pressure is p = 101 300 Pa. The resulting inlet Mach numbers are both approximately Ma = 0.019. Initially, the domain contains only exhaust gas. The test case is computed with a CFL number of 50. The lower limit for the preconditioned parameter is β^2_{min} = 1e-5.

The influence of low Mach preconditioning on the quality of the solution for different grid resolutions is analyzed. Starting with a 64 x 8 grid, it is successively refined up to a resolution of 2048 x 256. The air distribution at the outlet of the domain is used to assess the quality of the solution. The error is quantified as the L1-norm of the difference in the air distribution at the outlet compared to a reference solution.

$$Y_{\text{air, error}} = \frac{1}{n_y} \sum_{i=1}^{n_y} \left\| Y_{\text{air}} - Y_{\text{air, ref}} \right\|_i \tag{13}$$

Here, n_y is the number of grid points in y-direction, Y_{air} is the air mass fraction and $Y_{air, ref}$ is the reference air mass fraction. The reference for all computations is the preconditioned computation on the 2048 x 256 grid.

The cause for the deterioration of non-preconditioned computations is the unphysical behavior of the Roe solver at low Mach numbers [21]. With increasing mesh resolution, the artificial dissipation of the Roe solver vanishes, and the preconditioned and non-preconditioned computations should converge towards the same solution. The finest preconditioned computation can therefore be used as reference for the preconditioned as well as the non-preconditioned computations.

Figure 4 shows the L1-norm of the error in the air mass fraction at the outlet of the domain on different grids. As expected, the error of the non-preconditioned computation steadily decreases. Therefore, the non-preconditioned computation indeed converges towards the preconditioned solution for fine grids. Still, the non-preconditioned computations show significantly larger errors at equal mesh resolution. Without preconditioning, the grid needs to be at least 3 times finer, to lower the error to the same level as the preconditioned computation.

Figure 5 depicts the air distribution in the domain for a 128 x 16 grid. The increased dissipation of the non-preconditioned Roe solver leads to an exaggerated mixing of the gases, which results in a thicker mixing layer and therefore a larger error in the non-preconditioned computations.

Figure 6 shows the relative error of the mass flow at each iteration compared to its converged value at the outlet of the domain for a 256 x 32 grid. In the preconditioned computation, after 1565 iterations, the mass flow reaches a relative difference of 1e-3 to its converged value. The non-preconditioned computation requires 25000 iterations to reach the same level of convergence. A similar convergence acceleration can be observed for all grid refinements.

Low Pressure Turbine Rig

The 1.5 stage low pressure turbine rig "ATRD" (Advanced Turbine Research Demonstrator) was designed by MTU Aero Engines AG. This turbine has been extensively analyzed in previous publications using numerical methods [4, 26, 32, 33]. A broad base of measurements, carried out by MTU Aero Engines AG in cooperation with the Institute of Aircraft Propulsion Systems (ILA) at Stuttgart University, supports this purpose.

This paper focuses on a simplified configuration consisting of 1.5 stages (stator-rotor-stator) with a labyrinth seal at the tip and a small cavity at the hub of the rotor. The computational domain is represented in Fig. 7. The computed operating point has an inlet Mach number of Ma_{in} = 0.35 and an inlet Reynolds number of Re_{in} = 67000. The inlet Reynolds number is calculated based on the averaged state at the inlet of the turbine and the chord length of the first row.

The rotor is computed in a rotating frame of reference. The interfaces between rows are mixing planes based on band-wise flux averaged quantities. Steady one-dimensional NRBCs are applied at the inlet, outlet and mixing planes. At the inlet, radial distributions for the stagnation pressure, the stagnation temperature, the flow direction, the turbulent length scale and the turbulent intensity are prescribed. At the outlet, a radial pressure distribution is prescribed. The experiments and the computations were both performed using cold fluid. To avoid non-physical backflow near walls in the main flow, the first 2.5% channel height of each interface are merged to one band at hub and tip. The cavities are connected to the main flow using conservative non-matching interfaces, called zonal-mixed interfaces [34]. The tip cavity consists of a rotor section and a stator section, which are connected with a mixing plane. In the main flow region a low Reynolds approach is applied to the wall boundaries, while a wall function approach is used in the cavities. The blade, hub

FIGURE 5. AIR MASS FRACTION IN THE MIXING LAYER FOR A 128 X 16 GRID WITH (TOP) AND WITHOUT (BOTTOM) PRECONDITIONING.

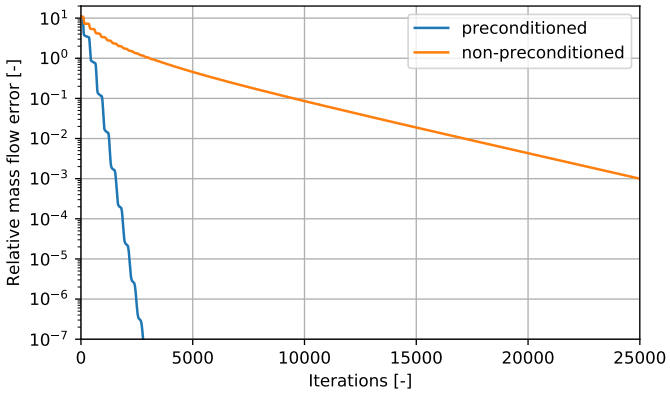

FIGURE 6. RELATIVE DIFFERENCE OF THE MASS FLOW AT EACH ITERATION AND THE CONVERGED VALUE AT THE OUTLET OF THE DOMAIN FOR A 256 X 32 GRID.

wall and tip wall of the rotor, as well as the inner wall of the labyrinth seal are rotating. All walls are adiabatic. For detailed information on the meshing setup, the reader is referred to [4].

The turbulence is modeled using the Menter SST turbulence model [35] in combination with the Kato Launder stagnation point fix [36]. Transition is modeled using the γ-Re_θ model [37]. The transition model is deactivated in the cavities.

Low Mach preconditioning is applied in the entire domain. In the main flow the lower limit for β^2 is set to $\beta^2_{\text{min}} = Ma^2_{\text{in}} = 0.1255$, where Ma_{in} is the inlet Mach number. This avoids instabilities arising from applying preconditioning to the boundary layer. In the cavities, where lower Mach numbers are expected, the lower limit is set to $\beta^2_{\text{min}} =$ 1e-3. Applying preconditioning to the mixing plane inside the cavity results in convergence issues. Therefore, $\beta^2 = 0.5 =$ const. is set in blocks next to the mixing plane.

First, the turbine is computed with air. Figure 8 compares the normalized pressure on the vane of the second stator com-

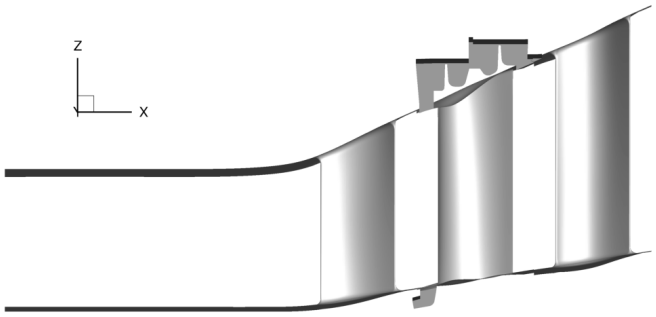

FIGURE 7. 1.5 STAGE LOW PRESSURE TURBINE RIG WITH TIP AND HUB CAVITIES.

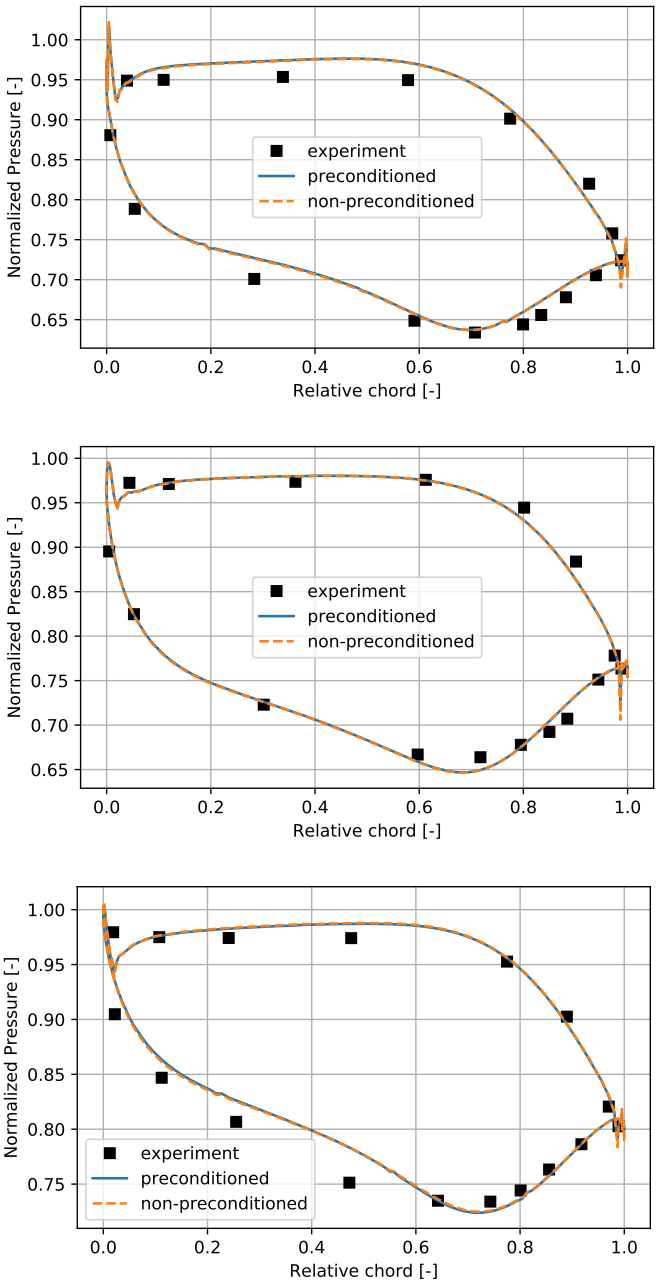

FIGURE 8. BLADE CUTS OF THE NORMALIZED PRESSURE IN THE SECOND STATOR AT THE RELATIVE CHANNEL HEIGHTS 10% (TOP), 50% (CENTER) AND 90% (BOTTOM).

puted by TRACE with experimental measurements. The normalized pressure is the ratio of the static pressure to the inlet stagnation pressure of the row at the same relative channel height. The numerical results are in good qualitative agreement with the experimental measurements.

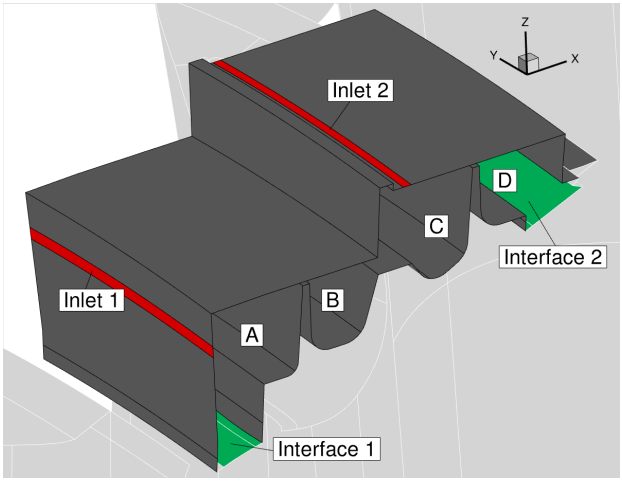

FIGURE 9. LOCATION OF AIR INLETS IN THE TIP CAVITY AND NAME CONVENTION FOR THE INTERFACES AND CHAMBERS OF THE LABYRINTH SEAL.

The application of low Mach preconditioning does not affect the solution significantly, since the local Mach number in the main gas path is larger than 0.35. It only results in a difference in normalized pressure of 0.2% on the suction side at 90% channel height.

The turbine rig is now computed using exhaust gas with two additional air inlets in the tip cavity. Figure 9 shows the position of the inlets and the naming conventions used in the following analysis. The mass flow prescribed at each inlet corresponds to 1% of the mass flow at the inlet of the turbine. The absolute stagnation temperature at the inlets is approximately equal to the average stagnation temperature at the inlet of the turbine.

Figure 10 shows the temperature difference between the walls of the labyrinth seal and the air inflow temperature. The application of low Mach preconditioning leads to a 12 K increase in the wall temperature of chamber B. The cause for this difference lies in the effect of low Mach preconditioning on the structure of the flow. Figure 11 shows the two-dimensional streamlines in an x-r-slice of the labyrinth seal. In chambers A, C and D, the location and size of the vortices remain consistent with and without preconditioning. In the non-preconditioned computation, the fluid from inlet 2 traverses chamber B, forming a thin vortex on the left side of the chamber and a large vortex on the right side. The fluid then exits through chamber A. With preconditioning, the positions of the vortices in chamber B are switched. The fluid from inlet 2 enters chamber B, but flows back to chamber C, thereby creating the smaller vortex on the right side. On the other side, fluid flows from chamber A to chamber B. Overall, this leads to a reduction of the mass flow through chamber B in the preconditioned case by a factor of four compared to the non-preconditioned case. The work introduced by the moving inner wall of the cavity cannot be conducted out of the chamber by the adiabatic walls. The reduction of the mass flow through chamber B leads to a reduced convective heat transfer, which leads to the increase in temperature inside the chamber.

Figure 12 compares the convergence of the error in the average air mass fraction at the interfaces between the labyrinth seal and the main flow. Here, the error is the difference between the current value at each iteration and the converged value. With preconditioning, the air mass fraction at interface 1 requires 9890 fewer iterations than the non-preconditioned computation to reach an error of 1e-3. This corresponds to a reduction of the number of required iterations to converge by 71.3%. At interface 2, preconditioning only reduces the number of required iterations by 33.3%. Further, at both interfaces, the preconditio-

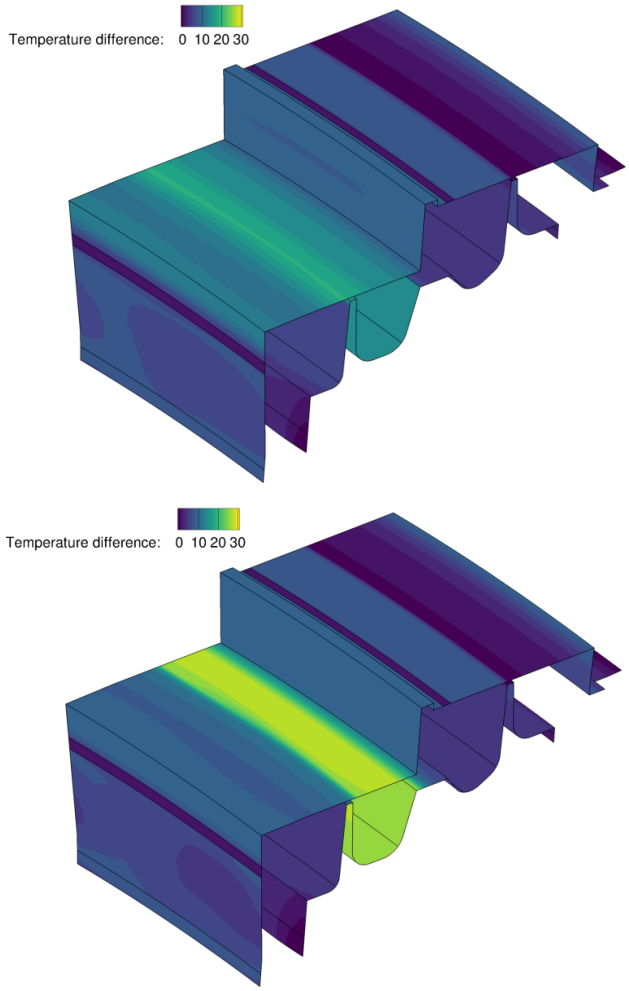

FIGURE 10. TEMPERATURE DIFFERENCE BETWEEN THE WALL TEMPERATURE AND THE AIR INFLOW TEMPERATURE IN THE LABYRINTH SEAL WITHOUT (TOP) AND WITH (BOTTOM) PRECONDITIONING.

ned computation predicts a reduction of the air mass fraction by approximately 9% compared to the non-preconditioned computation. This result is similar to the findings for the mixing layer test case, where the non-preconditioned Roe scheme leads to an exaggerated mixing of exhaust gas and air, and therefore higher air mass fractions on the side of the exhaust gas.

Figure 13 shows the error in the average stagnation temperature at the outlet of the turbine during the computations. The effect of the preconditioner on the overall convergence of the turbine is smaller than in the cavity, since the Mach number in the main flow is larger than 0.35. Still, the number of iterations needed to reduce the stagnation temperature error to 1e-3 decreases from 9315 to 7610. This is an acceleration by 18.3%.

CONCLUSION

This Paper presents the low Mach preconditioning method of the DLR's inhouse solver TRACE for multi-component thermally perfect gas.

The effectiveness of the preconditioner has been validated using two academic test cases. The lid driven cavity test case showed that preconditioning accelerated the convergence by 97%

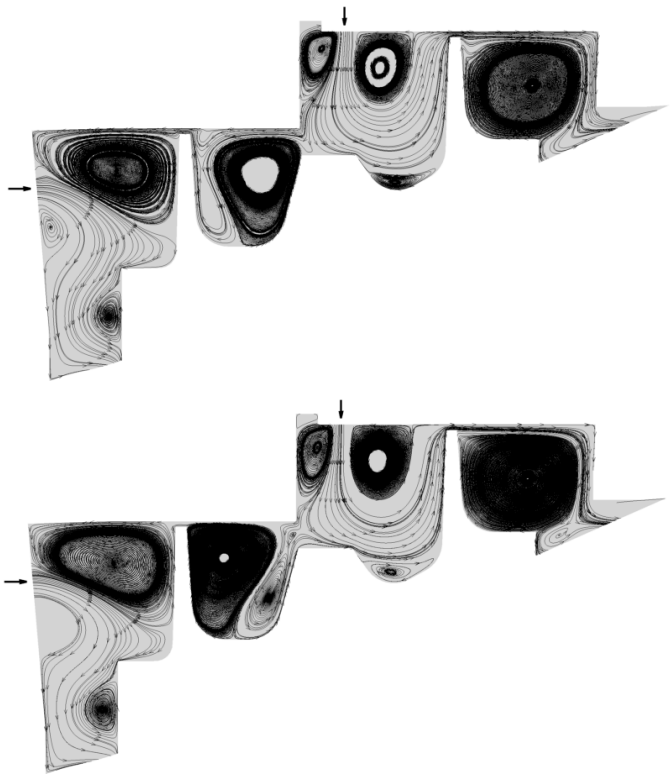

FIGURE 11. STREAMLINES IN THE LABYRINTH SEAL WITHOUT (TOP) AND WITH (BOTTOM) PRECONDITIONING. ARROWS INDICATE THE LOCATION OF THE AIR INLETS.

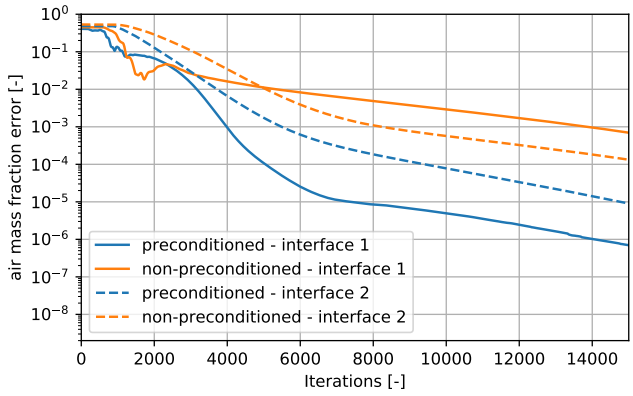

FIGURE 12. ERROR IN THE AIR MASS FRACTION AT INTERFACE 1 AND INTERFACE 2.

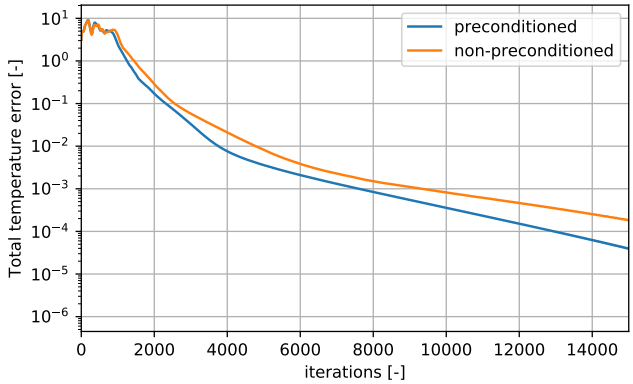

FIGURE 13. ERROR IN THE AVERAGE STAGNATION TEMPERATURE AT THE OUTLET OF THE TURBINE.

and greatly improved the quality of the solution. A grid refinement analysis of a laminar mixing layer of air and exhaust gas showed that the preconditioner reduces the grid-dependent error.

The preconditioner was applied to a low pressure turbine rig with a labyrinth seal. A first computation with air showed a good agreement with the experimental reference, both with and without preconditioning. The turbine rig was then computed with exhaust gas and two additional air inlets in the tip cavity. Here, low Mach preconditioning lead to changes in the flow structures inside the cavity, which resulted in a local increase in temperature by 12 K. Further, the preconditioned computation predicted a weaker propagation of air in the domain, compared to the non-preconditioned case. The computational time until convergence criteria were met was reduced by 33% for the cavity and by 18.3% for the outlet of the turbine.

ACKNOWLEDGMENT

The authors are grateful to MTU Aero Engines AG, for their co-sponsorship of the first author and for providing the low pressure turbine test case and the experimental data.

REFERENCES

[1] Rubechini, F., Marconcini, M., Arnone, A., Maritano, M., and Cecchi, S., 2008. "The impact of gas modeling in the numerical analysis of a multistage gas turbine". *Journal of Turbomachinery,* ***130***(2), mar.

[2] Young, J. B., and Wilcock, R. C., 2002. "Modeling the air-cooled gas turbine: Part 1—General thermodynamics". *Journal of Turbomachinery,* ***124***(2), apr, pp. 207–213.

[3] Fiedler, J., and di Mare, F., 2012. "Generalised implementation of low-Mach preconditioning for arbitrary three-dimensional geometries". In ECCOMAS 2012.

[4] Fiedler, J., Weber, A., Bosco, A., Engel, K., and di Mare, F., 2016. "Numerical simulation of the flow in the row labyrinth seal of an axial turbine using a low-Mach preconditioning technique". In Volume 2C: Turbomachinery, American Society of Mechanical Engineers.

[5] Chorin, A. J., 1967. "A numerical method for solving incompressible viscous flow problems". *Journal of Computational Physics,* ***2***(1), aug, pp. 12–26.

[6] Turkel, E., 1987. "Preconditioned methods for solving the incompressible and low speed compressible equations". *Journal of Computational Physics,* ***72***(2), oct, pp. 277–298.

[7] Choi, D., and Merkle, C. L., 1985. "Application of time-iterative schemes to incompressible flow". *AIAA Journal,* ***23***(10), oct, pp. 1518–1524.

[8] Choi, D., and Merkle, C. L., 1991. "Time-derivative preconditioning for viscous flows". In 22nd Fluid Dynamics, Plasma Dynamics and Lasers Conference, American Institute of Aeronautics and Astronautics.

[9] Buelow, P., Venkateswaran, S., and Merkle, C., 1995. "Grid aspect ratio effects on the convergence of upwind schemes". In 33rd Aerospace Sciences Meeting and Exhibit, American Institute of Aeronautics and Astronautics.

[10] Weiss, J. M., and Smith, W. A., 1995. "Preconditioning applied to variable and constant density flows". *AIAA Journal,* ***33***(11), nov, pp. 2050–2057.

[11] Venkateswaran, S., Weiss, J., Merkle, C., and Choi, Y.-H., 1992. "Propulsion-related flowfields using the preconditioned Navier-Stokes equations". In 28th Joint Propulsion Conference and Exhibit, American Institute of Aeronautics and Astronautics.

[12] Shuen, J.-S., Chen, K.-H., and Choi, Y., 1992. "A time-accurate algorithm for chemical non-equilibrium viscous flowsat all speeds". In 28th Joint Propulsion Conference and Exhibit, American Institute of Aeronautics and Astronautics.

[13] Li, D., Sankaran, V., Lindau, J., and Merkle, C., 2005. "A unfied computational formulation for multi-component and multi-phase flows". In 43rd AIAA Aerospace Sciences Meeting and Exhibit, p. 1391.

[14] Neaves, M. D., and Edwards, J. R., 2005. "All-speed time-accurate underwater projectile calculations using a preconditioning algorithm". *Journal of Fluids Engineering,* ***128***(2), pp. 284–296.

[15] Housman, J. A., Kiris, C. C., and Hafez, M. M., 2009. "Time-derivative preconditioning methods for multicomponent flows—part i: Riemann problems". *Journal of Applied Mechanics,* ***76***(2).

[16] Kiris, C. C., Housman, J. A., Barad, M. F., Brehm, C., Sozer, E., and Moini-Yekta, S., 2016. "Computational framework for launch, ascent, and vehicle aerodynamics (LAVA)". *Aerospace Science and Technology,* ***55***, pp. 189–219.

[17] Wu, J., Tang, L., Luke, E., and Cinnella, P., 2003. "A low mach number preconditioning scheme of the reactive roe flux". In 41st AIAA Aerospace Sciences Meeting and Exhibit.

[18] Elmahi, I., Gloth, O., Haenel, D., and Vilsmeier, R., 2008. "A preconditioned dual time-stepping method for combustion problems". *International Journal of Computational Fluid Dynamics,* ***22***(3), mar, pp. 169–181.

[19] Godfrey, A., Walters, R., and van Leer, B., 1993. "Preconditioning for the Navier-Stokes equations with finite-rate chemistry". In 31st Aerospace Sciences Meeting, American Institute of Aeronautics and Astronautics.

[20] Roe, P., 1981. "Approximate Riemann solvers, parameter vectors, and difference schemes". *Journal of Computational Physics,* ***43***(2), oct, pp. 357–372.

[21] Guillard, H., and Viozat, C., 1997. On the behavior of upwind schemes in the low Mach number limit. Tech. Rep. RR-3160, Apr.

[22] Turkel, E., 1999. "Preconditioning techniques in computational fluid dynamics". *Annual Review of Fluid Mechanics,* ***31***(1), pp. 385–416.

[23] Tweedt, D., Chima, R., Turkel, E., Tweedt, D., Chima, R., and Turkel, E., 1997. "Preconditioning for numerical simulation of low Mach number three-dimensional viscous turbomachinery flows". American Institute of Aeronautics and Astronautics.

[24] Anker, J. E., Mayer, J. F., and Stetter, H., 2002. "A preconditioned solution scheme for the computation of compressible flow in turbomachinery at arbitrary Mach number". *Task Quart.,* ***6***, Jan., pp. 143–176.

[25] Darmofal, D. L., and Siu, K., 1999. "A robust multigrid algorithm for the Euler equations with local preconditioning and semi-coarsening". *Journal of Computational Physics,*

151(2), may, pp. 728–756.

[26] Geiser, G., Wellner, J., Kügeler, E., Weber, A., and Moors, A., 2019. "On the simulation and spectral analysis of unsteady turbulence and transition effects in a multistage low pressure turbine".

[27] Becker, K., Heitkamp, K., and Kügeler, E., 2010. "Recent progress in a hybrid-grid CFD solver for turbomachinery flows". In V European Conference on Computational Fluid Dynamics ECCOMAS CFD 2010, J. C. F. Pereira, A. Sequeira, and J. M. C. Pereira, eds.

[28] Erturk, E., Corke, T. C., and Gökçöl, C., 2005. "Numerical solutions of 2-D steady incompressible driven cavity flow at high Reynolds numbers". *International Journal for Numerical Methods in Fluids,* ***48***(7), pp. 747–774.

[29] Ghia, U., Ghia, K. N., and Shin, C. T., 1982. "High-Re solutions for incompressible flow using the Navier-Stokes equations and a multigrid method". pp. 387–411.

[30] Kost, F., and Rehder, H.-J., 2018. Exakte Berechnung der Mischung von Gasströmen bei idealen Gasen mit variabler Wärmekapazität und Anwendung auf gekühlte Turbinengitter. September.

[31] Giles, M. B., 1988. Non-reflecting boundary conditions for the Euler equations. Tech. rep. CFDL Report 88-1.

[32] Geiser, G., Wellner, J., Kügeler, E., Weber, A., and Moors, A., 2018. "On the simulation of unsteady turbulence and transition effects in a multistage low pressure turbine, part II: Full-wheel simulation". In ASME 2018 Turbo Expo. HGF - Research field: Aeronautics, Space and Transport HGF - Program: Aeronautics HGF - Program Themes: propulsion systems DLR - Program: L ER - Engine Research.

[33] Kügeler, E., Geiser, G., Wellner, J., Weber, A., and Moors, A., 2018. "On the simulation of unsteady turbulence and transition effects in a multistage low pressure turbine, part III: Comparison of harmonic balance and full wheel simulation". In ASME 2018 Turbo Expo.

[34] Yang, H., Nuernberger, D., Nicke, E., and Weber, A., 2003. "Numerical investigation of casing treatment mechanisms with a conservative mixed-cell approach". ASMEDC.

[35] Menter, F. R., Kuntz, M., and Langtry, R., 2003. "Ten years of industrial experience with the SST turbulence model".

[36] Kato, M., 1993. "The modeling of turbulent flow around stationary and vibrating square cylinders". In 9th Symposium on Turbulent Shear Flows.

[37] Menter, F. R., Langtry, R. B., Likki, S. R., Suzen, Y. B., Huang, P. G., and Voölker, S., 2006. "A correlation-based transition model using local variables—Part I: Model formulation". p. 413.

Appendix: Transformation Matrices

The differential of the pressure for thermally perfect gas reads

$$dp = \rho\,(\gamma-1)\,de + \sum_{i=1}^{N}\left((\gamma-1)\,(e-e_i)+R_iT\right)d\rho_i. \tag{14}$$

Here, $\gamma = c_p/c_v$ is the specific heat ratio, R_i is the specific gas constant of species i, ρ_i is the partial density of species i and e is the specific internal energy, which is related to the specific energy by

$$E = e + \frac{1}{2}\left(u^2+v^2+w^2-(\Omega r)^2\right), \tag{15}$$

where, Ω is the rotational speed and r is the radius. Further, e is the mass-weighted sum of the species' internal energy

$$e = \sum_{i=1}^{N} Y_i e_i. \tag{16}$$

The specific enthalpy is

$$h = e + \frac{p}{\rho} \tag{17}$$

and the specific heat capacities at constant pressure and constant volume, respectively are

$$c_p = \left.\frac{\partial h}{\partial T}\right|_{Y_i} \tag{18}$$

$$c_v = \left.\frac{\partial e}{\partial T}\right|_{Y_i}. \tag{19}$$

The thermal gas equation is

$$p = \sum_{i=1}^{N} \rho_i R_i T. \tag{20}$$

Finally, with the differential of the entropy

$$TdS = de - \frac{p}{\rho^2}d\rho, \tag{21}$$

the transformation matrices between conservative and entropy primitive variables can be calculated as

$$\frac{\partial Q_S}{\partial Q} = \begin{pmatrix} (\gamma-1)\left(q^2-E\right) & -u(\gamma-1) & -v(\gamma-1) & -w(\gamma-1) & (\gamma-1) & C_1 & \dots & C_N \\ -\frac{u}{\rho} & \frac{1}{\rho} & 0 & 0 & 0 & 0 & \dots & 0 \\ -\frac{v}{\rho} & 0 & \frac{1}{\rho} & 0 & 0 & 0 & \dots & 0 \\ -\frac{w}{\rho} & 0 & 0 & \frac{1}{\rho} & 0 & 0 & \dots & 0 \\ \frac{1}{\rho T}\left(q^2-H\right) & -\frac{u}{\rho T} & -\frac{v}{\rho T} & -\frac{v}{\rho T} & \frac{1}{\rho T} & 0 & \dots & 0 \\ -\frac{Y_1}{\rho} & 0 & 0 & 0 & 0 & \frac{1}{\rho} & \dots & 0 \\ \vdots & \vdots & \vdots & \vdots & \vdots & \vdots & \ddots & \vdots \\ -\frac{Y_N}{\rho} & 0 & 0 & 0 & 0 & 0 & \dots & \frac{1}{\rho} \end{pmatrix} \tag{22}$$

$$\frac{\partial Q}{\partial Q_S} = \begin{pmatrix} \frac{1}{a^2} & 0 & 0 & 0 & -\frac{\rho}{c_p} & -\rho\frac{C_1}{a^2} & \dots & -\rho\frac{C_N}{a^2} \\ \frac{u}{a^2} & \rho & 0 & 0 & -\frac{\rho u}{c_p} & -u\rho\frac{C_1}{a^2} & \dots & -u\rho\frac{C_N}{a^2} \\ \frac{v}{a^2} & 0 & \rho & 0 & -\frac{\rho v}{c_p} & -v\rho\frac{C_1}{a^2} & \dots & -v\rho\frac{C_N}{a^2} \\ \frac{w}{a^2} & 0 & 0 & \rho & -\frac{\rho w}{c_p} & -w\rho\frac{C_1}{a^2} & \dots & -w\rho\frac{C_N}{a^2} \\ \frac{H}{a^2} & u\rho & v\rho & w\rho & -\frac{\rho}{c_p}\left(\frac{a^2}{\gamma-1}-H\right) & -H\rho\frac{C_1}{a^2} & \dots & -H\rho\frac{C_N}{a^2} \\ \frac{Y_1}{a^2} & 0 & 0 & 0 & -\frac{\rho Y_1}{c_p} & \rho\left(1-Y_1\rho\frac{C_1}{a^2}\right) & \dots & -Y_1\rho\frac{C_N}{a^2} \\ \vdots & \vdots & \vdots & \vdots & \vdots & \vdots & \ddots & \vdots \\ \frac{Y_N}{a^2} & 0 & 0 & 0 & -\frac{\rho Y_N}{c_p} & -Y_N\rho\frac{C_1}{a^2} & \dots & \rho\left(1-Y_N\rho\frac{C_N}{a^2}\right) \end{pmatrix}, \tag{23}$$

with

$$C_i = (\gamma-1)\left(e-e_i\right) + R_i T. \tag{24}$$

Further, H is the total specific enthalpy

$$H = E + \frac{p}{\rho} \tag{25}$$

and

$$q^2 = u^2 + v^2 + w^2. \tag{26}$$

The conservative preconditioning matrix is calculated as:

$$P^{-1} = \frac{\partial Q}{\partial Q_S} P_S^{-1} \frac{\partial Q_S}{\partial Q}, \tag{27}$$

with

$$P^{-1} = I + \frac{\left(\frac{1}{\beta^2}-1\right)}{a^2} \begin{pmatrix} A_1 & A_2 & A_3 & A_4 & A_5 & C_1 & \dots & C_\mathrm{N} \\ uA_1 & uA_2 & uA_3 & uA_4 & uA_5 & uC_1 & \dots & uC_\mathrm{N} \\ vA_1 & vA_2 & vA_3 & vA_4 & vA_5 & vC_1 & \dots & vC_\mathrm{N} \\ wA_1 & wA_2 & wA_3 & wA_4 & wA_5 & wC_1 & \dots & wC_\mathrm{N} \\ HA_1 & HA_2 & HA_3 & HA_4 & HA_5 & HC_1 & \dots & HC_\mathrm{N} \\ Y_1A_1 & Y_1A_2 & Y_1A_3 & Y_1A_4 & Y_1A_5 & Y_1C_1 & \dots & Y_1C_\mathrm{N} \\ \vdots & \vdots & \vdots & \vdots & \vdots & \vdots & \ddots & \vdots \\ Y_\mathrm{N}A_1 & Y_\mathrm{N}A_2 & Y_\mathrm{N}A_3 & Y_\mathrm{N}A_4 & Y_\mathrm{N}A_5 & Y_\mathrm{N}C_1 & \dots & Y_\mathrm{N}C_\mathrm{N} \end{pmatrix}, \tag{28}$$

where

$$A_1 = (\gamma-1)\left(q^2-E\right) \tag{29}$$
$$A_2 = -(\gamma-1)\,u \tag{30}$$
$$A_3 = -(\gamma-1)\,v \tag{31}$$
$$A_4 = -(\gamma-1)\,w \tag{32}$$
$$A_5 = (\gamma-1). \tag{33}$$

I is the identity matrix.

Appendix: Preconditioned Roe Matrix

The preconditioned Roe matrix $P^{-1}|\tilde{PD}|$ used in (12) is constructed by performing an eigenvector decomposition of the preconditioned jacobian

$$P^{-1}|\tilde{PD}| = P^{-1} M |\Lambda| M^{-1}. \tag{34}$$

Here, M and M^{-1} are the right and left eigenvector matrices of PD and $|\Lambda|$ is a diagonal matrix containing the absolute preconditioned eigenvalues (9). In this work, the following definitions

have been used:

$$M^{-1} = \begin{pmatrix} n_x + \frac{n_z v}{a} - \frac{n_y w}{a} - \frac{n_x A_1}{a^2} & -\frac{n_x A_2}{a^2} & -\frac{n_z}{a} - \frac{n_x A_3}{a^2} \\ n_y - \frac{n_z u}{a} + \frac{n_x w}{a} - \frac{n_y A_1}{a^2} & \frac{n_z}{a} - \frac{n_y A_2}{a^2} & -\frac{n_y A_3}{a^2} \\ n_z + \frac{n_y u}{a} - \frac{n_x v}{a} - \frac{n_z A_1}{a^2} & -\frac{n_y}{a} - \frac{n_z A_2}{a^2} & \frac{n_x}{a} - \frac{n_z A_3}{a^2} \\ -\frac{U}{\rho} - \frac{A_1 d_{14}}{\rho a^2 \beta^2} & \frac{n_x}{\rho} - \frac{A_2 d_{14}}{\rho a^2 \beta^2} & \frac{n_y}{\rho} - \frac{A_3 d_{14}}{\rho a^2 \beta^2} \\ \frac{U}{\rho} + \frac{A_1 d_{15}}{\rho a^2 \beta^2} & -\frac{n_x}{\rho} + \frac{A_2 d_{15}}{\rho a^2 \beta^2} & -\frac{n_y}{\rho} + \frac{A_3 d_{15}}{\rho a^2 \beta^2} \\ -\frac{Y_1}{\rho} & 0 & 0 \\ \vdots & \vdots & \vdots \\ -\frac{Y_N}{\rho} & 0 & 0 \end{pmatrix}$$

$$\begin{pmatrix} \frac{n_y}{a} - \frac{n_x A_4}{a^2} & -\frac{n_x A_5}{a^2} & \frac{n_x \varepsilon_1 (\gamma-1)}{a^2} & \dots & \frac{n_x \varepsilon_N (\gamma-1)}{a^2} \\ -\frac{n_x}{a} - \frac{n_y A_4}{\rho} & -\frac{n_y A_5}{a^2} & \frac{n_y \varepsilon_1 (\gamma-1)}{a^2} & \dots & \frac{n_y \varepsilon_N (\gamma-1)}{a^2} \\ -\frac{n_z A_4}{a^2} & -\frac{n_z A_5}{a^2} & \frac{n_z \varepsilon_1 (\gamma-1)}{a^2} & \dots & \frac{n_z \varepsilon_N (\gamma-1)}{a^2} \\ \frac{n_z}{\rho} - \frac{A_4 d_{14}}{\rho a^2 \beta^2} & -\frac{A_5 d_{14}}{\rho a^2 \beta^2} & \frac{\varepsilon_1 (\gamma-1) d_{14}}{\rho a^2 \beta^2} & \dots & \frac{\varepsilon_N (\gamma-1) d_{14}}{\rho a^2 \beta^2} \\ -\frac{n_z}{\rho} + \frac{A_4 d_{15}}{\rho a^2 \beta^2} & \frac{A_5 d_{15}}{\rho a^2 \beta^2} & -\frac{\varepsilon_1 (\gamma-1) d_{15}}{\rho a^2 \beta^2} & \dots & -\frac{\varepsilon_N (\gamma-1) d_{15}}{\rho a^2 \beta^2} \\ 0 & 0 & \frac{1}{\rho} & \dots & 0 \\ \vdots & \vdots & \vdots & \ddots & \vdots \\ 0 & 0 & 0 & \dots & \frac{1}{\rho} \end{pmatrix} \tag{35}$$

$$M = \begin{pmatrix} n_x & n_y & n_z \\ u n_x & u n_y + a n_z & u n_z - a n_y \\ v n_x - a n_z & v n_y & v n_z + a n_x \\ w n_x + a n_y & w n_y - a n_x & w n_z \\ \varepsilon n_x - a v n_z + a w n_y & \varepsilon n_y + a u n_z - a w n_x & \varepsilon n_z - a u n_y + a v n_x \\ Y_1 n_x & Y_1 n_y & Y_1 n_z \\ \vdots & \vdots & \vdots \\ Y_N n_x & Y_N n_y & Y_N n_z \end{pmatrix}$$

$$\begin{pmatrix} \frac{\rho \beta^2}{d_{45}} & \frac{\rho \beta^2}{d_{45}} & 0 & \dots & 0 \\ \frac{\rho}{d_{45}} \left(u\beta^2 + n_x d_{15} \right) & \frac{\rho}{d_{45}} \left(u\beta^2 + n_x d_{14} \right) & 0 & \dots & 0 \\ \frac{\rho}{d_{45}} \left(v\beta^2 + n_y d_{15} \right) & \frac{\rho}{d_{45}} \left(v\beta^2 + n_y d_{14} \right) & 0 & \dots & 0 \\ \frac{\rho}{d_{45}} \left(w\beta^2 + n_z d_{15} \right) & \frac{\rho}{d_{45}} \left(w\beta^2 + n_z d_{14} \right) & 0 & \dots & 0 \\ \frac{\rho}{d_{45}} \left(H\beta^2 + U d_{15} \right) & \frac{\rho}{d_{45}} \left(H\beta^2 + U d_{14} \right) & \rho \varepsilon_1 & \dots & \rho \varepsilon_N \\ \frac{\rho}{d_{45}} Y_1 \beta^2 & \frac{\rho}{d_{45}} Y_1 \beta^2 & \rho & \dots & 0 \\ \vdots & \vdots & \vdots & \ddots & \vdots \\ \frac{\rho}{d_{45}} Y_N \beta^2 & \frac{\rho}{d_{45}} Y_N \beta^2 & 0 & \dots & \rho \end{pmatrix}, \tag{36}$$

with

$$\varepsilon = E - \frac{RT}{\gamma - 1}, \quad \varepsilon_i = e_i - \frac{R_i T}{\gamma - 1} \tag{37}$$

and

$$d_{14} = \lambda_1 - \lambda_4, \tag{38}$$

$$d_{15} = \lambda_1 - \lambda_5, \tag{39}$$

$$d_{45} = \lambda_4 - \lambda_5. \tag{40}$$